JOURNAL OF GEOPHYSICAL RESEARCH, VOL. 102, NO. C11, PAGES 25,091–25,099, NOVEMBER 15, 1997

A comparison of theory and laboratory measurements of wave propagation and attenuation in grease ice

Karl Newyear and Seelye Martin

School of Oceanography, University of Washington, Seattle

Abstract. In an experimental study using a wave tank in a laboratory cold room we determine the dispersion relation and amplitude attenuation for surface waves propagating through different thicknesses of grease ice. We compare our results to two ice rheology models: the mass-loading model, which predicts a wavelength decrease relative to open water, and an infinite depth viscous fluid model, which predicts an increasing wavelength as the wave Reynolds number decreases. For a thick grease ice layer in which the waves are strongly damped we observe that the wavelength increases by up to 30% over its open water value in the frequency range of 1.0 Hz $< f <$ 1.6 Hz. This trend agrees with the viscous model, and the agreement improves as the ice thickness increases and at higher wave frequencies where conditions approach those of the infinite depth approximation. The Reynolds number decreases approximately exponentially with frequency and is in the range $1 < R < 10$ for our experimental conditions. From the model the inferred viscosity of grease ice is at least 4 orders of magnitude larger than the open water value and increases with frequency, suggesting that grease ice is non-Newtonian. For the observed parameter values our analysis shows that the mass-loading model of grease ice is inapplicable while a one-layer viscous model provides a better match to laboratory observations.

1. Introduction

Grease ice is a suspension of frazil crystals, which are small ice discs or spicules measuring ~ 1-4 mm in diameter and 1-100 μm in thickness that form in turbulent, slightly supercooled water [see *Martin and Kauffman*, 1981, Figure 11]. "The disc-like shape is the result of a highly anisotropic surface energy" of the ice crystal structure [*Weeks and Ackley*, 1982, p. 13]. As the number density of crystals increases, a "dense slurry of the individual frazil platelets" forms, "with concentrations by volume in sea-water of 20-40%," which at the surface has the visual appearance of a grease or oil slick [*Martin and Kauffman*, 1981, p. 284]. *Martin* [1981] reports grease ice thicknesses of 0.1-0.3 m in the Bering Sea.

Weitz and Keller [1950] and *Peters* [1950] give the first quantitative description of wave propagation through grease ice by treating the ice as a layer of noninteracting point masses. Using this mass-loading model, they each solve for the two-dimensional velocity potential in an inviscid fluid with mixed surface boundary conditions in which waves propagate from open water across a distinct ice edge into ice-covered water. Both papers predict that phase speed and wavelength decrease as waves enter the ice. In a field application, *Wadhams and Holt* [1991] use this theory to estimate grease and pancake ice thickness from the wavelength change observed using satellite synthetic aperture radar (SAR) imagery.

Martin and Kauffman [1981] discuss the related phenomena of wave attenuation and find from laboratory experiments that a nonlinear viscosity explains observations of wave damping in grease ice. Their data suggest that wave amplitude decays linearly with distance according to a frequency-dependent slope and that the ice is a thixotropic (shear-thinning) fluid in which viscosity decreases as the shear rate increases. *Tsang* [1982] suggests that a natural frazil slush in a canal possesses an "apparent viscosity" which leads to high hydraulic resistance. *Weber* [1987] models the effect of brash ice with a Lagrangian formulation for waves propagating in a two-layer fluid. He describes the upper layer as having Newtonian viscosity, while the lower layer is inviscid and infinitely deep. For the upper layer he assumes a balance between pressure and friction, which implies a wave Reynolds number R which is much less than 1. For the limit of a thin, very viscous upper layer this model leads to an exponential wave decay rate and an increase in wave damping with frequency. This agrees with field observations that an ice cover acts as a low-pass filter and that high-frequency waves are reflected or damped out within a short distance of the ice edge [*Hunkins*, 1962; *Liu et al.*, 1991a, b; *Squire et al.*, 1995]. In recent work, J. Keller (Gravity waves on ice-covered water, submitted to the *Journal of Geophysical Research*, 1997) (hereinafter referred to as Keller, submitted manuscript, 1997) describes a two-layer system where each layer has an arbitrary thickness, the upper layer is viscous, and the lower layer is inviscid.

The present paper describes a laboratory study of wave propagation and decay in grease ice and compares the results to the mass-loading model and an infinite depth viscous model of wave propagation. In what follows, section 2 describes our experimental procedures, and section 3 explains our data analysis methods. Section 4 discusses the mass-loading model and derives the viscous fluid model, both used to describe wave propagation in grease ice. Section 5 compares our results with the theories, and section 6 discusses the implications of our results, addressing issues of scaling and applicability to field situations. Finally, section 7 summarizes our conclusions.

2. The Experiment

2.1. Apparatus

Figure 1 shows the laboratory apparatus. The wave tank is a flat-bottomed rectangular box, ~ 3.5 m long, 1 m wide, and 1 m

Paper number 97JC02091.
0148-0227/97/97JC-02091$09.00

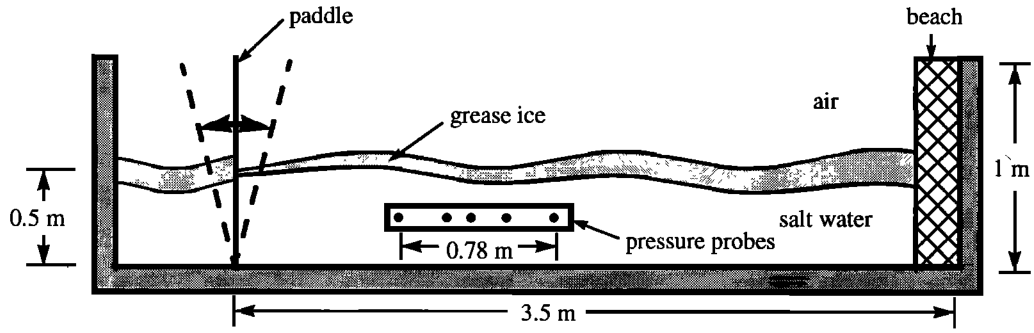

Figure 1. A schematic side view of the laboratory tank, approximately to scale.

deep, located in a cold room. One of the long sides is made of transparent Plexiglas, allowing a side view of the wave propagation and ice thickness. The tank walls and bottom are thermally insulated with Styrofoam sheets so that the water is cooled from above by regulating the room air temperature with a digital thermostat to $\pm 1^{\circ}$ C. We generate waves with a flap-type paddle, which consists of a sheet of plywood, hinged at the bottom edge and extending the width of the tank. It is driven by a variable speed dc motor with an eccentric wheel, allowing the generation of waves over a range of frequencies and amplitudes. The beach is horsehair packing material (sheets of densely packed interwoven fibers held together with plastic mesh). We fill the tank to a depth of ~ 0.5 m with a solution of water and rock salt (NaCl) at a salinity comparable to Arctic surface waters (around 33 practical salinity units (psu)).

We measure wave properties with five independent strain gauge probes, each producing a time series of analog voltage that is subsequently digitized for analysis. The instruments are attached to a metal frame at precisely known separation distances and at a uniform depth of ~ 0.225 m along the center line of the tank. To avoid aliasing, the relative probe spacing is unequal such that probe 1 is located at the origin, probe 2 is at 0.217 m, probe 3 is at 0.345 m, probe 4 is at 0.517 m; and probe 5 is at 0.781 m. The probe ports are positioned to point horizontally across the tank, perpendicular to the wave vector to eliminate pressure anomalies caused by dynamic pressure fluctuations. Thus we measure only those pressure perturbations caused by the wave propagation.

2.2. Procedure

For each experiment we cool the room temperature for several days until the salt water reaches its freezing point. We initiate ice growth by rapidly dropping the air temperature to ~ -10° C and generating waves with the paddle to provide turbulence, a condition necessary for frazil formation [*Martin*, 1981]. In this way the ice layer thickness grows at a rate of up to 1.5 cm h^{-1}. When the ice reaches the desired thickness, we return the air temperature to near freezing, measure wave propagation with the probes, and make various observations of the ice properties.

As the layer thickness and ice concentration increase, waves are attenuated so severely that the signal amplitude becomes too small and our data quality is compromised. For thicker layers (up to 0.2 m) the frazil crystals cohere into domains with dimensions of a few centimeters, called flocs. When these flocs form in the ice above the probes, we terminate the experiment and melt the ice.

The grease ice layer is described in terms of its thickness h, salinity S, and volume concentration c. We measure c by scooping up a portion of the bulk ice/brine layer, filtering the solid from the liquid, then allowing the samples to melt and warm to room temperature. We calculate c from the relative volumes of each, taking into account the density difference between ice and water; observed values of c range from 0.22 to 0.57. We measure salinity using an optical salinometer, which is accurate to within 0.1 psu. The ice salinity ranges from 6.0 to 21.0 psu while that of the liquid water ranges from 33.0 to 37.8 psu, where the variation in water salinity is due to salt conservation in our tank.

As Figure 1 shows schematically, the ice thickness profile in our experiments was not uniform; the ice layer increased in thickness away from the paddle. This is attributable to inviscid Stokes drift and radiation stress caused by viscous wave decay [*Phillips*, 1966; *Martin and Kauffman*, 1981; *Longuet-Higgins and Stewart*, 1964], which causes the grease ice to move in a downwave direction and pile up against the beach. *Bauer and Martin* [1983] present a numerical model of grease ice growth and herding. They predict a wedge-shaped accumulation of grease ice with a maximum thickness of 0.1-0.3 m at the downwind edge of leads for a wind speed of 5-10 m s^{-1} and fetch of 50-500 m, which is consistent with the field observations of *Martin* [1981]. Because neither the mass-loading nor viscous models account for a nonuniform ice layer thickness, we estimate a spatially averaged thickness by measuring h with a ruler through the transparent Plexiglas tank wall when no waves are present. Observed values range from 0.05 to 0.2 m. Given h and the ice concentration c, the product ch has dimensions of length and is termed the effective ice thickness.

2.3. Data Collection

We ran two sets of experiments, each comprised of several sets of runs made under varying ice conditions. A run is a single pressure time series for a fixed paddle frequency. On completion of a run we changed the paddle frequency and performed another run under the same ice conditions. A set consists of all runs made with the same ice thickness on the same day. Between runs we made qualitative observations of such processes as wave splashing or downtank herding of the ice by waves. Occasionally, we recorded several consecutive runs at the same frequency to ensure consistent results. We usually ran two sets of runs per day, one in the morning and one in the afternoon, each requiring about 2.5 hours to complete. If the ice conditions were unchanged from morning to afternoon, then we considered all runs on that day as a single set. In each set we keep only those runs for which the waves experience no significant reflection from the beach; if reflections do occur, we require that the reflected waves damp out completely before propagating back through the array. The presence or absence of reflected waves was determined visually and later confirmed by checking that the signal amplitude decayed monotonically away from the paddle. Between sets we grew more ice by lowering the cold room air temperature.

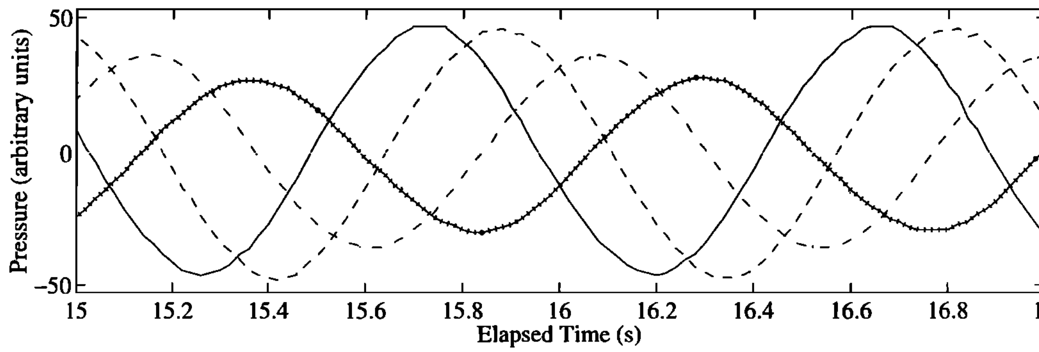

Figure 2. A portion of a typical data time series, where the vertical axis has arbitrary units of pressure. Data from probe 1 is shown by the solid line; probe 2 is shown by the dashed line; probe 3 is shown by the dotted line; probe 4 is shown by the dash-dot line; and probe 5 is shown by the hatched solid line.

3. Data Analysis

3.1. Frequency and Time Delay

Figure 2 shows a portion of the raw data for one run, illustrating that the signal is offset in time from one probe to the next and that its amplitude decreases away from the paddle. For this case, waves are propagating through 0.11 m of grease ice (ch=5.4 cm), and the exponential wave damping coefficient is $q = 0.33\ \mathrm{m}^{-1}$. For each run we apply a one-dimensional fast Fourier transform (FFT) and use the Welch method [*Oppenheim and Schafer*, 1975, pp. 553-554] to obtain the power spectral density and phase transfer function for each probe. We assume that the wave is monochromatic at the frequency f_M of the maximum in the power spectral density. Although frequency resolution improves with FFT size, practical time constraints limit the data record length. We recorded data at a rate of 50 Hz for 44 s per run, which permits use of a 2048 point FFT. The phase transfer function is evaluated at f_M to find the phase delay θ_m of the signal at probe m relative to that at probe 1, where probe 1 is closest to the paddle and probe 5 is farthest away. The time offset of each signal is calculated as

$$t_m = \frac{\theta_m}{2\pi f_M} \qquad t_1 = 0 \tag{1}$$

We derive the signal amplitudes P_m from the power spectrum by using Parseval's theorem [*Oppenheim and Schafer*, 1975, pp. 390-391].

3.2. Wavenumber and Decay Coefficient

Knowing f_M, t_m, and the probe locations x_m, the wave phase speed $c_{p,m}$ between probes 1 and m is expressed as

$$c_{p,m} = \frac{x_m}{t_m} \qquad \text{or} \qquad c_{p,m} = \frac{\omega}{k_m} \tag{2}$$

We rewrite (2) to give the real part of the wavenumber as

$$k_m = \frac{\omega t_m}{x_m} = \frac{2\pi f_M t_m}{x_m} \tag{3}$$

We estimate the error in k_m from uncertainties in the observed quantities. This method requires data from only two probes, so for each run we use the pair with the largest separation distance for which both signal amplitudes are significantly above the estimated noise level. This minimizes the relative error caused by uncertainties in t_m and x_m. At very high frequencies this procedure becomes untenable because the waves are so quickly attenuated that no pair of probes has sufficiently strong signals. The measure-

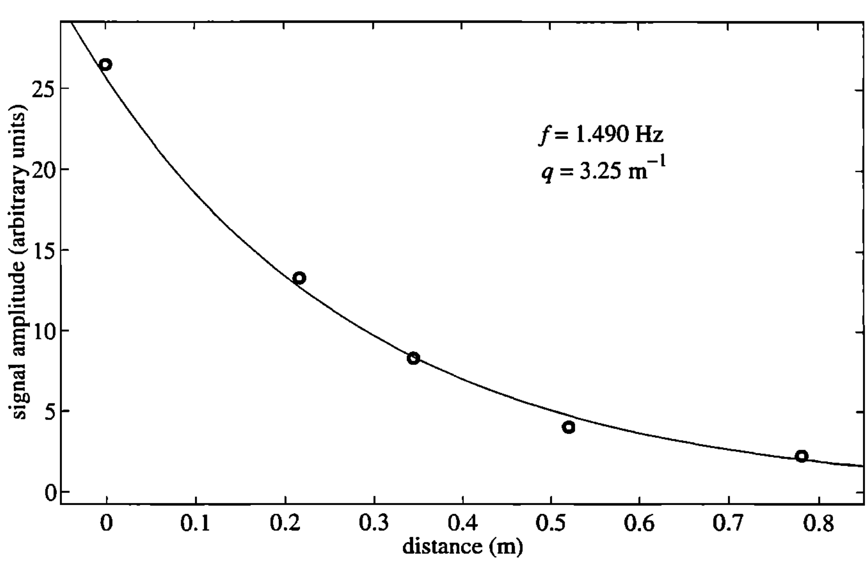

Figure 3. An example of signal amplitude versus distance with best fit exponential curve.

Table 1. Observed and Derived Variables for Experiment 1

Frequency (f), Hz	Open Water Wavenumber (k_0), m^{-1}	Observed Wavenumber (k), m^{-1}	Decay Coefficient (q), m^{-1}	Reynolds Number (R)	Viscosity (ν), 10^{-2} $m^2 s^{-1}$
1.173	5.54	5.45	1.07	4.5	1.35
1.176	5.57	5.54	1.05	4.7	1.27
1.181	5.62	5.46	1.14	4.1	1.42
1.185	5.65	5.49	1.12	4.2	1.38
1.187	5.68	5.47	1.08	4.3	1.34
1.196	5.76	5.52	1.08	4.3	1.32
1.284	6.63	6.22	1.87	2.8	1.64
1.296	6.76	6.40	1.78	3.0	1.47
1.424	8.16	7.00	2.77	1.9	1.75
1.504	9.11	8.22	3.45	2.0	1.42
1.514	9.23	8.13	3.22	2.0	1.38
1.517	9.26	8.22	3.54	1.9	1.45

The ice thickness is 11.3 cm, and ch=5.4 cm. For the variables the 95% confidence limits are ± 0.09 m^{-1} for k, ± 0.03 m^{-1} for q, ± 0.1 for R, and $\pm 0.08 \times 10^{-2}$ $m^2 s^{-1}$ for ν.

ments are further hindered at high f because the amplitude of a pressure perturbation at the water surface, measured at depth, decreases for shorter wavelengths while the instrument noise remains constant, so the signal-to-noise ratio is reduced. In our analysis we assume that the wave attenuation takes the form

$$P \propto \exp[-qx] \tag{4}$$

We calculate the decay coefficient q by fitting a line to the observed signal amplitude P when plotted as $\ln(P)$ versus x at each f_M, similar to the procedure used by *Wadhams et al.* [1988]. The negative slope of the least squares fit is q (q must be positive while the slope is negative). We find a posteriori that the assumption of exponential decay given in (4) is generally valid (Figure 3).

In our experiments we found two sets of runs suitable for analysis; these were done at effective ice thicknesses of ch=5.4 and 6.9 cm. For these thicknesses, Tables 1 and 2 list the dimensional values of the open water wavenumber and the observed values of k and q as a function of frequency. Our other runs were unsuitable because for a very thin ice layer we observed multiple wave reflections from the beach and paddle, while for a very thick layer the waves damped out before passing over the probe array. Additionally, flocs quickly formed from thick grease ice. Our second set of useful runs was terminated because of the formation of flocs; otherwise, the two sets of results presented here pertain only to grease ice.

4. Models

Squire [1993] derives both the mass-loading and elastic plate models of sea ice in detail, noting on page 219 that they are nearly equivalent, "the mass-loading model may be regarded as the limit of an elastic plate with no rigidity." However, when applied to ice typical of the marginal ice zone (MIZ), *Squire* [1995, p. 997] states that the elastic plate formulation "is being used in a manner for which it was not intended, and there are concomitant dangers if its predictions are taken too far." Therefore we do not invoke the elastic plate model to explain our observations. Instead, because of the

Table 2. Observed and Derived Variables for Experiment 2

Frequency (f), Hz	Open Water Wavenumber (k_0), m^{-1}	Observed Wavenumber (k), m^{-1}	Decay Coefficient (q), m^{-1}	Reynolds Number (R)	Viscosity (ν) 10^{-2} $m^2 s^{-1}$
1.053	4.47	4.41	0.82	4.7	1.75
1.054	4.48	4.42	0.84	4.6	1.79
1.054	4.48	4.42	0.85	4.6	1.80
1.109	4.95	4.88	1.26	3.5	2.06
1.209	5.88	5.47	1.74	2.6	2.09
1.285	6.65	5.83	2.32	2.0	2.30
1.288	6.67	5.89	2.36	2.0	2.27
1.299	6.79	5.93	2.36	2.0	2.25
1.395	7.84	6.26	2.94	1.5	2.36
1.440	8.35	6.43	3.10	1.4	2.34
1.490	8.93	6.79	3.25	1.4	2.16
1.490	8.94	6.81	3.41	1.3	2.19
1.510	9.18	6.73	3.18	1.3	2.22

The ice thickness is 14.6 cm, and ch = 6.9 cm. See Table 1 for confidence limits.

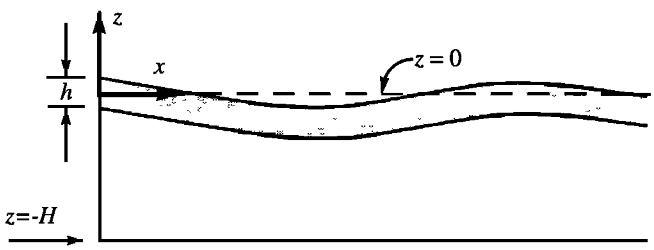

Figure 4. The coordinate system used in the wave propagation models.

viscous decay theorized by *Weber* [1987] and observed by *Martin and Kauffman* [1981], we use the model presented by *Stokes* [1851] and *Lamb* [1932, pp. 623-628], which describes time-decaying waves in an infinitely deep fluid with constant Newtonian viscosity ν; the solution admits both wave attenuation and a wavelength increase. We briefly review both models and state the results.

We assume that small-amplitude, monochromatic plane waves propagate in an incompressible fluid, and we solve for the two-dimensional velocity field. Our coordinate system is the vertical x-z plane shown in Figure 4 in which waves propagate to the right and u and w are the velocity components. For the mass-loading model the fluid is irrotational, inviscid, and of uniform depth H with an ice layer of thickness h, while for the viscous model the fluid is infinitely deep and homogeneous. At the free surface the boundary conditions for both cases are the linearized kinematic condition

$$\left.\frac{\partial\phi}{\partial z}\right|_{z=0} = \frac{\partial\eta}{\partial t} \tag{5}$$

and the linearized Bernoulli equation

$$\left.\frac{\partial\phi}{\partial t}\right|_{z=0} = \frac{1}{\rho}P|_{z=0} + gz \tag{6}$$

where ϕ is the velocity potential, η is the free surface displacement, P is the pressure field, ρ is the density, and g is the gravitational acceleration. We use the convention that wave frequency f, measured in hertz, is real while the wavenumber κ is complex

$$\kappa = k + iq \tag{7}$$

where κ, k, and q have units of m^{-1}. This treats wave attenuation as an exponential, spatial decay given by the magnitude of q. The real part of the wavenumber for ice-free deep water is

$$k_0 = \frac{\omega^2}{g} = \frac{4\pi^2 f^2}{g} \tag{8}$$

where $\omega = 2\pi f$.

4.1. The Mass-Loading Model

For a finite depth H, there is no normal flow at the bottom

$$\left.\frac{\partial\phi}{\partial z}\right|_{z=-H} = 0 \tag{9}$$

The ice field is imposed via the top boundary condition rather than any bulk fluid property and is parameterized by the ice thickness h, the volume fraction of ice c, and the density ρ_i. In the mass-loading model the frazil crystals are assumed to be noninteracting, and the condition of zero rigidity

$$P|_{z=0} = \rho_i ch\frac{\partial^2\eta}{\partial t^2} \tag{10}$$

yields the dispersion relation

$$\omega^2 = \frac{gk\rho_w \tanh(kH)}{\rho_w + \rho_i chk\tanh(kH)} \tag{11}$$

When ice is absent, $ch = 0$ and (11) reduces to the open water dispersion relation

$$\omega^2 = gk_0 \tanh(k_0 H) \tag{12}$$

For any given wave frequency the mass-loading model yields a larger wavenumber than for open water. At small wavenumbers it asymptotically approaches the open water value; at larger wavenumbers it strongly diverges.

4.2. The Viscous Model

From *Lamb*'s [1932, sections 348 and 349] version of *Stokes*'s [1851] problem for wave propagation in an infinitely deep viscous fluid we write

$$u = \frac{-\partial\phi}{\partial x} - \frac{\partial\psi}{\partial z} \qquad v = \frac{-\partial\phi}{\partial z} + \frac{\partial\psi}{\partial x} \tag{13}$$

provided that

$$\nabla^2\phi = 0 \qquad \frac{\partial\psi}{\partial t} = \nu\nabla^2\psi \tag{14}$$

where ψ is the stream function. The boundary conditions include the vanishing of both components of surface stress

$$\left.\frac{\partial\phi}{\partial t}\right|_{z=0} - g\eta + 2\nu\left.\frac{\partial w}{\partial z}\right|_{z=0} = 0 \tag{15}$$

$$\nu\left.\left(\frac{\partial w}{\partial x} + \frac{\partial u}{\partial z}\right)\right|_{z=0} = 0 \tag{16}$$

and that the solution is bounded at depth

$$\lim_{z\to-\infty}\phi = 0 \tag{17}$$

Neglecting surface tension, we rewrite *Lamb*'s [1932] solution to describe a wave decaying with distance and obtain the complex dispersion relation

$$\left(2\nu\kappa^2 - i\omega\right)^2 + g\kappa = 4\nu^2\kappa^3\left(\kappa^2 - \frac{i\omega}{\nu}\right)^{1/2} \tag{18}$$

We define the complex, nondimensional wavenumber X as

$$X = \frac{\kappa}{k_0} = \hat{k} + i\hat{q} \tag{19}$$

where

$$\hat{k} = \frac{k}{k_0} \qquad \hat{q} = \frac{q}{k_0} \tag{20}$$

are dimensionless forms of the wavenumber and damping coefficient. We also define the wave Reynolds number R by using the wave phase speed $U = \frac{\omega}{k_0}$ and wavelength $\lambda = \frac{2\pi}{k_0}$ to obtain

$$R = \frac{\omega}{4\nu k_0^2} = \frac{g^2}{4\nu\omega^3} \tag{21}$$

which is a function of ω and ν only. Using (19) and (21), we rewrite (18) in nondimensional form as

$$\frac{i}{4R^3}X^6 - \frac{1}{2R^2}\left(X^5 + 3X^4\right) + \frac{2i}{R}\left(X^3 - X^2\right)$$
$$-X^2 + 2X - 1 = 0 \qquad (22)$$

Given R, (22) yields six roots for X. As R varies, the roots trace out curves in the complex plane, three of which lie in the quadrant where $\hat{k}$ and $\hat{q}$ are positive. In this region we obtain a power series solution to (22) for large R

$$X \approx 1 + \frac{i}{R} + \frac{\sqrt{2}}{4}\frac{(1-i)}{R^{3/2}} - \frac{9}{4R^2} + \frac{41}{16\sqrt{2}}\frac{(1+i)}{R^{5/2}} + \cdots \qquad (23)$$

As we show below, this particular expansion is an approximation to that root of (22) which is closest to our experimental data.

Figure 5 shows both the exact ((22), solid lines) and approximate ((23), dashed line) solutions for $0.1 < R < 50$, omitting the four exact solutions which do not converge to the inviscid solution of $\hat{k} = 1$, $\hat{q} = 0$. As labeled, the dots mark the location of the solutions for $R = 0.1$, and the hatch marks show the values for $R = 0.5$, 1, 2, 5, 10, and 15. The vertical dotted line shows $\hat{k} = 1$, which corresponds to the open water wavelength. Examination of the figure shows that as R becomes large, the two solid curves approach the real axis along the line $\hat{k} = 1$. This vertical approach to the $\hat{k}$ axis means that as R increases, the waves attain their open water wavelength before damping ceases to occur. Equation (23) also shows that the first damping term is of order R^{-1} while the first term giving a wavelength change is of order $R^{-3/2}$. Thus for $R \gg 1$, damping can occur without a change in wavelength.

4.3. Reynolds Number and Viscosity

Obtaining results from the viscous model requires the evaluation of ν or, equivalently, of the Reynolds number. For each experimental run we determine R by comparison of the observed values of $X_{obs} = \hat{k}_{obs} + i\hat{q}_{obs}$ with the solution curves from (22). At each observed frequency the closest solution $\hat{k}_\nu + i\hat{q}_\nu$ is found by minimizing the expression

$$d = \sqrt{\left(\hat{k}_{obs} - \hat{k}_\nu\right)^2 + \left(\hat{q}_{obs} - \hat{q}_\nu\right)^2} \qquad (24)$$

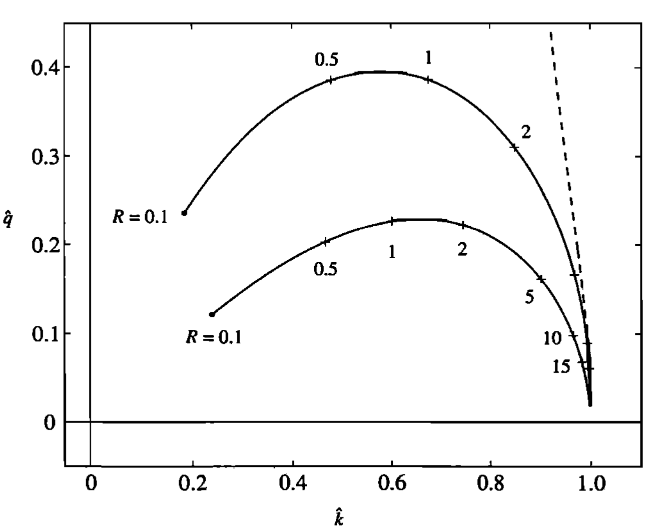

Figure 5. Solutions of (22) for positive ($\hat{k}$, $\hat{q}$). See text for additional description.

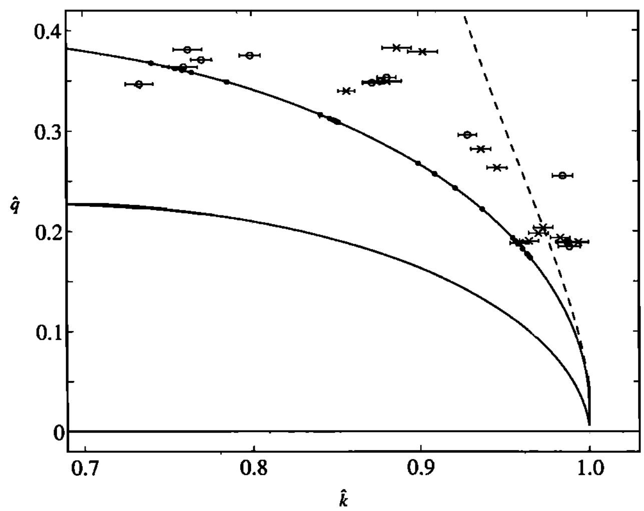

Figure 6. Comparison of the solution curves and the observed values of X. Solid lines are the exact solutions (equation (22)), the dashed line is the approximate solution (equation (23)). The crosses show the solutions for ch=5.4 cm, and the open circles are for 6.9 cm, all with 95% confidence limits. The dots on the solution curves are the closest solution for each X. See text for additional description.

Figure 6 shows the solution curves from Figure 5 (on a different scale), our experimental observations with their 95% confidence limits, and the set of closest solutions from the viscous theory. Although the trend of our observations in this figure is similar to the theory, our data generally lie above the curves indicating that for a given wavelength the wave damping is greater than predicted. Only for small values of R (i.e., farthest to the left) does the theory match our observations of both $\hat{k}$ and $\hat{q}$ simultaneously. Figure 6 also shows that $\hat{k} < 1$ for all our observations. All of the closest viscous solutions are located on the upper of the two solid curves, and each is associated with a value of R, while each X_{obs} corresponds to a specific f. Thus we obtain a value of R for each frequency. Once R is known, we calculate the viscosity ν from (21). We then define the relative viscosity

$$\hat{\nu} = \frac{\nu}{\nu_0} \qquad (25)$$

where ν_0 is taken as the pure water viscosity of 10^{-6} m^{2}s^{-1}. Tables 1 and 2 also list these derived values of R and ν.

5. Results

From *Kinsman* [1965, pp. 131-132], waves in a fluid of depth h^* are deep water waves when the phase speed equals 95% of its deep water value. This occurs for $k_0 h^* \approx \frac{\pi}{2}$ or, equivalently, when

$$f(h^*) \equiv f_c(h^*) = \sqrt{\frac{g}{8\pi h^*}} \qquad (26)$$

When h^* equals the tank depth H, then all our observed waves are deep water waves. For the viscous theory to be applicable, however, h^* should equal the grease ice thickness h. Therefore we define the nondimensional frequency $\hat{f}$ as

$$\hat{f} = \frac{f}{f_c(h)} \qquad (27)$$

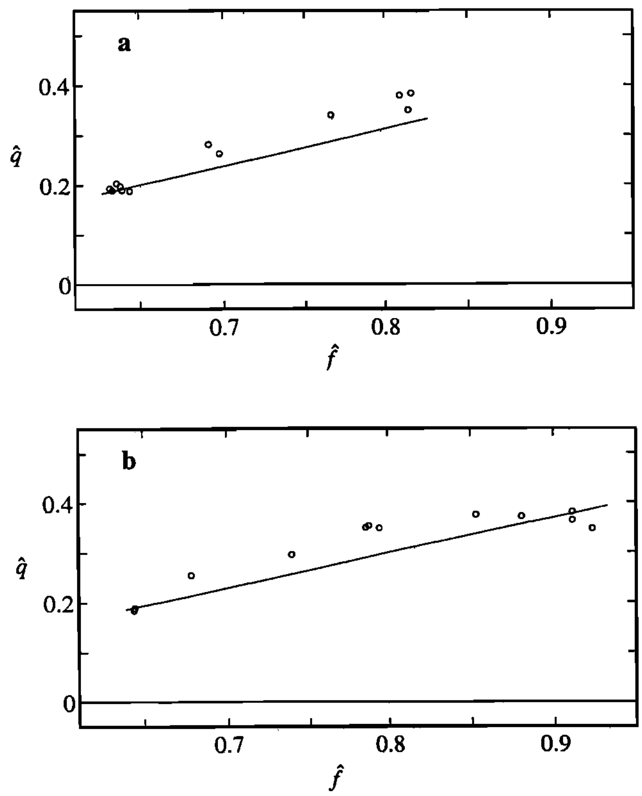

Figure 7. Wave decay coefficient $\hat{q}$ versus $\hat{f}$. (a) ch=5.4 cm; (b) ch=6.9 cm. See text for additional description.

When $\hat{f} \geq 1$, the wave speed is at least 95% of its deep water value, so we expect the viscous model to strictly apply. For $\hat{f} < 1$ we expect the deep water solution to diverge from our observations. For the first experiment, described in Table 1, f_c = 1.85 Hz and $0.63 \leq \hat{f} \leq 0.82$; for the second experiment, shown in Table 2, f_c = 1.63 and $0.64 \leq \hat{f} \leq 0.93$. This indicates that $\hat{f} < 1$ for all our runs, but $\hat{f} \to 1$ at the higher frequencies.

Figures 7 through 10 present our results plotted versus $\hat{f}$; the upper frame in each figure is for ch = 5.4 cm, the lower frame is for ch = 6.9 cm. Figures 7a and 7b plot the wave decay coefficient ^ versus $\hat{f}$. On these figures the open circles give our observations, where in all cases the 95% confidence limits lie within the circles. The solid line in each subfigure gives the viscous solution derived by the method described in section 4.3. Examination of Figure 7 shows that in both cases, $\hat{q}$ is approximately linearly proportional to $\hat{f}$ and that the slope is similar in both cases. For low frequency waves, $\hat{q}$ is small, and damping becomes unimportant. Thus the grease ice cover serves as a low-pass filter for wave energy. At high $\hat{f}$ the shorter waves are severely damped; we observe an e-folding decay distance as small as half a wavelength for $\hat{f} \approx 0.9$.

Figures 8a and 8b show the dependence of the Reynolds number R on $\hat{f}$. The solid circles are our observations with their 95% error bars, and the line is the least squares exponential curve fit to those points. For reference we show a solid horizontal line at R = 1. For all our observations, $1 < R < 10$ so that inertial effects and viscous effects are comparable. Our measurements at large R have greater errors because of weak wave damping, which leads to experimental difficulties such as partial standing waves. As $\hat{f}$ increases, R decreases exponentially and approaches R = 1 as $\hat{f}$ approaches 1, indicating that viscous effects are important for high-frequency waves

Figures 9a and 9b show the log of normalized viscosity $\hat{v}$. In each figure the error bars are smaller than the symbols, and the line is the least squares linear fit. The figures show that viscosity increases with $\hat{f}$, is always more than 4 orders of magnitude greater than that of water, and is larger for thicker ice. Our experiments yield values of $\hat{v}$ as large as 2.4×10^4. A Newtonian fluid has constant viscosity; our observation that $\hat{v}$ increases with $\hat{f}$ implies that grease ice is non-Newtonian.

Finally, Figures 10a and 10b show $\hat{k}$ as a function of $\hat{f}$. Our observations and their uncertainty are given by the open circles. The viscous solution is shown as a solid line and the mass-loading solution as a dashed line. Because the mass-loading model yields such large values of $\hat{k}$, we use a discontinuous vertical axis to include them. For all frequencies we find $\hat{k} < 1$, indicating that the wavenumber is smaller and the wavelength is longer than for open water. For increasing $\hat{f}$, $\hat{k}$ decreases approximately linearly, so that the wavelength relative to its open water value becomes longer as the frequency increases. As $\hat{f}$ decreases, R increases and $\hat{k} \to 1$, signifying that the wavelength is unaffected by the ice. However, at low frequencies we find nonnegligible decay ($\hat{q} \approx 0.2$), so that the waves are damped with very little wavelength change in accordance with (23). At higher frequencies ($\hat{f} > 0.85$), where the wavelength change is largest, the viscous model matches our observations. Therefore the viscous model accurately describes the change in wavelength when the ice layer approximates a deep fluid. In contrast, the mass-loading model is inapplicable to our experiment since it predicts $\hat{k} > 1$ for our experimental frequencies.

6. Discussion

Figure 10 shows that the mass-loading model is inapplicable to our observations and that the viscous model comes closer to explaining our observations, both in terms of wave damping and

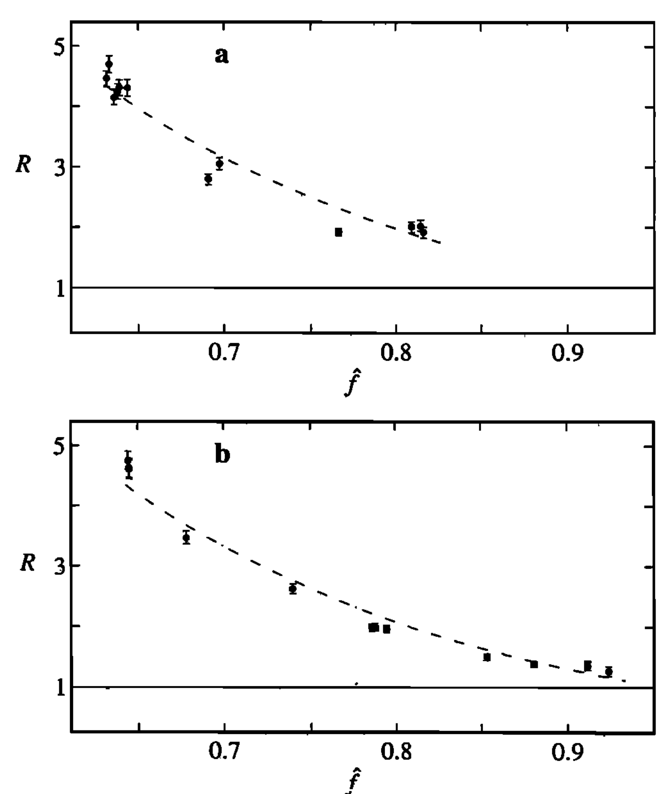

Figure 8. Reynolds number R versus f. (a) ch=5.4 cm; (b) ch=6.9 cm.

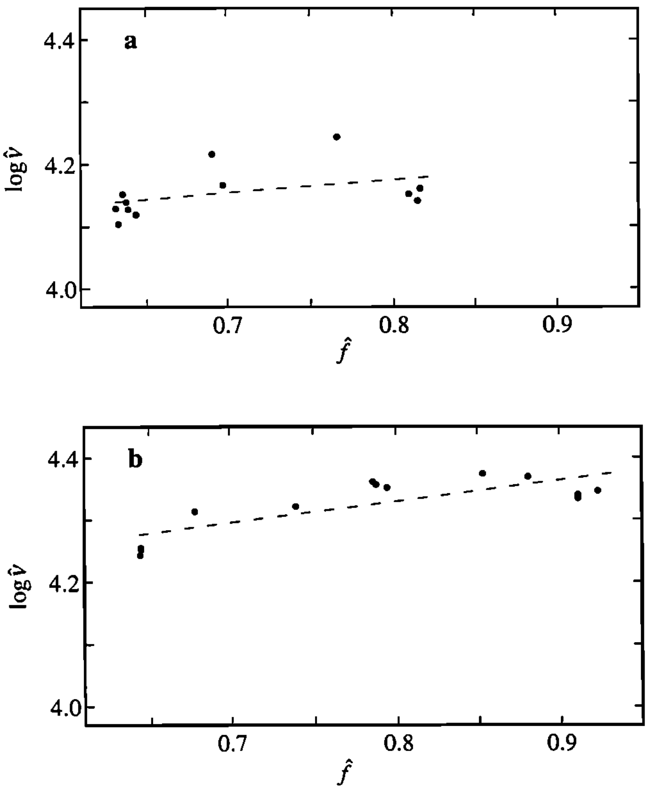

Figure 9. Log of normalized viscosity $\hat{\nu}$ versus $\hat{f}$. (a) ch=5.4 cm; (b) ch=6.9 cm.

wavelength change. Why this is so deserves a closer examination. The large implied viscosity in Figure 9 suggests that frazil crystals at concentrations approaching $c = 0.5$ strongly interact, possibly through sintering, collisions, and/or shearing, thus violating the noninteraction assumption of the mass-loading model. The viscous model also has shortcomings. Our experiments take place in a fluid system which is clearly nonhomogeneous and where the grease ice layer does not always satisfy the deep water approximation given by (26). At low $\hat{f}$ the model generally underpredicts wave damping and overpredicts a change in wavelength. However, as $\hat{f}$ approaches 1, the deep water condition is more nearly satisfied in our experiments, and as Figure 10b shows, the agreement between theory and observations is best at the highest $\hat{f}$ where the relative ice thickness kh is largest. To address the shortcomings of the infinite depth theory, it will be necessary to employ a two-layer viscous model such as Keller (submitted manuscript, 1997), described earlier. Further, because of the apparent variability of $\hat{\nu}$ with frequency as discussed above, it may also be necessary to use a non-Newtonian form of viscosity or a viscoelastic/viscoplastic ice rheology.

Despite the difficulty in scaling our results for waves of the order of meters to sea swell typical of the outer MIZ where grease ice is often found, we can directly compare our results to wind waves generated in leads where grease ice is forming. Our laboratory frazil crystals are "life-sized" and need no scaling, as is the case when attempting to compare our laboratory results to an ice field with larger ice floes. Further, because our laboratory ice layer thicknesses are comparable to those observed in the field, as noted earlier, the bulk properties of grease ice are well replicated in the laboratory. The waves we generate are of the order of 1 Hz, and waves of this frequency are common in leads of a few hundreds of meters across [*Martin and Kauffman*, 1981; *Bauer and Martin*, 1983].

The rapid damping of short-period waves also has implications for remote sensing of the MIZ. As noted in *Wadhams and Holt* [1991], areas covered with grease ice appear dark in SAR imagery because Bragg-resonant waves in the ice are damped out very quickly in accord with our laboratory results in Figure 7. This low-pass filter allows only the longer wavelengths to enter and propagate through the areas of grease ice. The lack of short, steep waves leads to a relatively smooth sea surface and allows the rapid formation of large areas of pancake ice floes, as reported by *Wadhams et al.* [1996] for the Greenland Sea Odden region.

7. Conclusions

Laboratory measurements of the propagation and damping of surface gravity waves over a range of frequencies in a field of grease ice with varying effective thicknesses ch show that wave damping is exponential with distance and is frequency-dependent; $\hat{q}$ is small for low wave frequencies and increases with $\hat{f}$ at high frequencies. The wave Reynolds number is O(1) and is an exponentially decreasing function of $\hat{f}$. The derived bulk viscosity of grease ice is at least 4 orders of magnitude larger than for water and

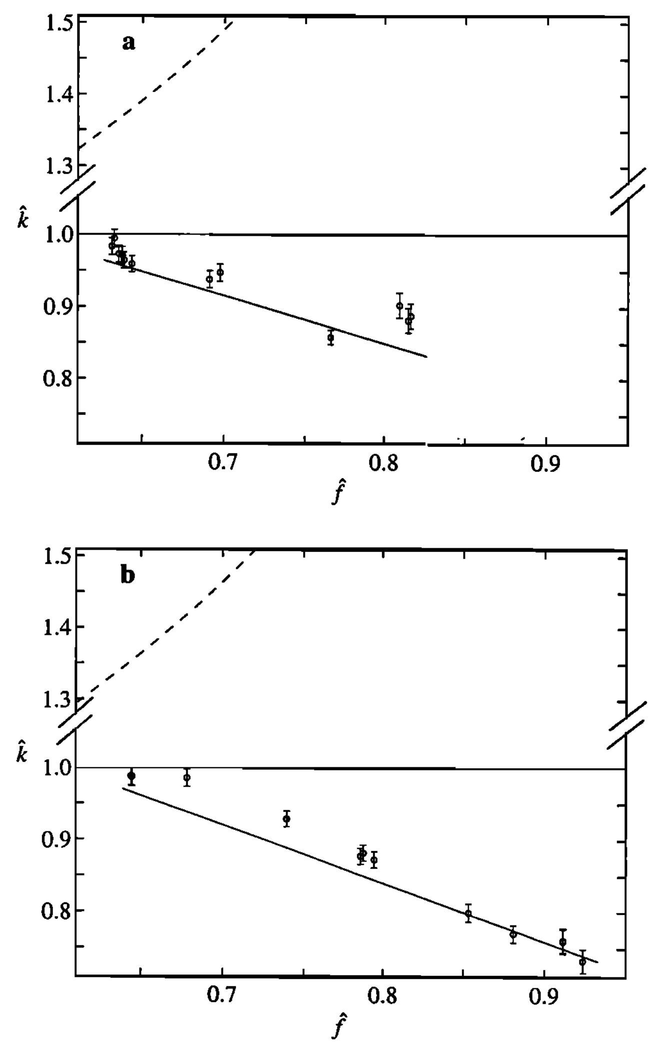

Figure 10. Normalized wavenumber $\hat{k}$ versus $\hat{f}$. (a) ch=5.4 cm; (b) ch=6.9 cm.

increases with frequency, implying that grease ice behaves as a non-Newtonian fluid. Because of the observed wave lengthening, the mass-loading model prediction of a significant wavelength shortening relative to open water is inapplicable to grease ice at our observed wave frequencies. At high frequencies an infinite depth Newtonian fluid model of grease ice yields good agreement with the data and explains both the observed wave attenuation and wavelength increase, while at lower frequencies the results diverge from the theory. Models which may improve on our results include a viscoelastic or a two-layer viscous model of the ice/water system.

Acknowledgments. The authors gratefully acknowledge the support of the Office of Naval Research under ONR contract N00014-90-J-0161. We thank Joseph Keller for timely and helpful suggestions regarding viscous fluids, Peter Kauffman for designing the pressure probes, and Peter Kauffman and Randy Fabro for constructing them. We also thank Robert Drucker for writing the software used in our primary data analysis and Meredith Fort for laboratory assistance. Publication 2184, School of Oceanography, University of Washington.

References

Bauer, J., and S. Martin, A model of grease ice growth in small leads, *J. Geophys. Res., 88*, 2917-2925, 1983.

Hunkins, K., Waves on the Arctic Ocean, *J. Geophys. Res., 67*, 2477-2489, 1962.

Kinsman, B., *Wind Waves: Their Generation and Propagation on the Ocean Surface*, 75 pp., Prentice-Hall, Englewood Cliffs, N. J., 1965.

Lamb, H., *Hydrodynamics*, 738 pp., Dover, Mineola, N. Y., 1932.

Liu, A., P. Vachon, and C. Peng, Observation of wave refraction at an ice edge by synthetic aperture radar, *J. Geophys. Res., 96*, 4803-4808, 1991a.

Liu, A., B. Holt, and P. Vachon, Wave propagation in the marginal ice zone: Model predictions and comparisons with buoy and synthetic aperture radar data, *J. Geophys. Res., 96*, 4605-4621, 1991b.

Longuet-Higgins, M.S., and R.W. Stewart, Radiation stresses in water waves: A physical discussion with applications, *Deep Sea Res. Oceanogr. Abstr., 11*, 529-562, 1964.

Martin, S., Frazil ice in rivers and oceans, *Annu. Rev. Fluid Mech., 13*, 379-397, 1981.

Martin, S., and P. Kauffman, A field and laboratory study of wave damping by grease ice, *J. Glaciol., 27*, 283-313, 1981.

Oppenheim, A. and R. Schafer, *Digital Signal Processing*, 585 pp., Prentice-Hall, Englewood Cliffs, N. J., 1975.

Peters, A.S., The effect of a floating mat on water waves, *Commun. Pure Appl. Math., 3*, 319-354, 1950.

Phillips, O.M., *The Dynamics of the Upper Ocean*, 261 pp., Cambridge Univ. Press, Cambridge, 1966.

Squire, V., A comparison of the mass-loading and elastic plate models of an ice field, *Cold Reg. Sci. Technol., 21*, 219-229, 1993.

Squire, V., Geophysical and oceanographic information in the marginal ice zone from ocean wave measurements, *J. Geophys. Res., 100*, 997-998, 1995.

Squire, V., J. Dugan, P. Wadhams, P. Rottier, and A. Liu, Of ocean waves and sea ice, *Annu. Rev. Fluid Mech., 27*, 115-168, 1995.

Stokes, G., On the effect of internal friction in causing the motion of a fluid to subside: Application to the case of oscillatory waves, *Trans. Cambridge Philos. Soc., 9, 2*, 57-62, 1851. (Reprinted in Mathematical and Physical Papers, vol. 3, 415 pp., Cambridge Univ. Press, New York, 1922.)

Tsang, G., Resistance of Beauharnois Canal in winter, *J. Hydraul. Div. Am. Soc. Civ. Eng., 108*, 167-186,1982.

Wadhams, P., and B. Holt, Waves in frazil and pancake ice and their detection in Seasat synthetic aperture radar imagery, *J. Geophys. Res., 96*, 8835-8852, 1991.

Wadhams, P., V. Squire, D. Goodman, A. Cowan, and S. Moore, The attenuation rates of ocean waves in the marginal ice zone, *J. Geophys. Res., 93*, 6799-6818, 1988.

Wadhams, P., J. Comiso, E. Prussen, S. Wells, M. Brandon, E. Aldworth, T. Viehoff, R. Allegrino, and D. Crane, The development of the Odden ice tongue in the Greenland Sea during winter 1993 from remote sensing and field observations, *J. Geophys. Res., 101*, 18213-18235, 1996.

Weber, J.E., Wave attenuation and wave drift in the marginal ice zone, *J. Phys. Oceanogr., 17*, 2351-2361, 1987.

Weeks, W. and S. Ackley, The Growth, Structure, and Properties of Sea Ice, *Monogr. 82-1*, 130 pp., U.S. Army Cold Reg. Res. and Eng. Lab., Hanover, N. H., 1982

Weitz, M. and J. Keller, Reflection of water waves from floating ice in water of finite depth, *Commun. Pure Appl. Math., 3*, 305-318, 1950.

S. Martin and K. Newyear, School of Oceanography, Box 35740, University of Washington, Seattle, WA 98195-7940. (e-mail: seelye@ocean.washington.edu; karl@ocean.washington.edu)

(Received November 1, 1996; revised March 12, 1997; accepted July 16, 1997.)